Experimental investigation on the hydrodynamic performance of a pile-supported OWC-type breakwater

Yusuf R. Almalki, Ioannis Karmpadakis, and Chris Swan

Abstract—**The present study considers the design optimisation of an Oscillating Water Column (OWC) incorporated into a pile-supported breakwater structure. This has been achieved by performing a substantial number of scaled physical model tests and a methodical variation of key device parameters within multiple configurations. The key aspects that have been investigated include: (a) the geometric characteristics of the breakwater structure, (b) the pneumatic efficiency of the OWC, (c) the geometry of the OWC chamber and (d) the relative position of the OWC chamber within the breakwater. The present work considers (monochromatic) regular waves of varying steepness and effective water depth as incident wave conditions. The efficiency of the designed structure in terms of shore protection capacity and wave energy extraction was assessed by quantifying relevant transmission coefficients and the power output metrics. This has been achieved by using a combination of collocated and complementary measuring devices, such as arrays of wave gauges, pressure transducers and a high-definition video camera. The study concluded that systematic refinement of the geometrical parameters can substantially enhance the overall hydrodynamic efficiency of a pile-supported OWC breakwater. Additionally, it was found that a configuration featuring a chamber positioned in front of the breakwater, with a relative chamber breadth $b_c b^{-1}$ of 0.67, outperforms wider breadth configurations in terms of both energy extraction efficiency and reduction of the transmission coefficient. Taken together, the present study provides an in-depth analysis of the effects of key design parameters of a breakwater–integrated OWC, its efficiency and shore protection potential.**

Index Terms—**Wave energy, Oscillating water column, Pile-supported breakwater ...**

I. Introduction

THE integration of oscillating water columns (abbreviated as OWC hereafter) into wave breakwaters has been a rising design choice to promote a multi-use structure that can utilise wave energy and provide coastal protection. This design concept holds significant promise as it enables cost and infrastructure sharing while leveraging the performance of the structure through the synergistic nature of this coupling. The presence of OWCs has been shown by [1] to enhance the wave attenuation capabilities of breakwaters. This concept has the potential to improve the economic competitiveness and viability of OWCs, ultimately contributing to the emergence of wave energy in the energy market.

The concept is not particularly new, [2] studied the integration of OWCs into caisson-type breakwaters. This study was followed by field tests conducted at the port of Sakura [3]. The integration of OWCs into bottom-set caissons was further investigated by [4]–[6], and [7]. The integration of OWCs into pile-supported breakwaters, however, has been experimentally studied in [8], which conducted experiments with a configuration featuring a finite lip to validate the work presented in [9]. More recently, [10] conducted a laboratory experiment on a pile-supported OWC and investigated the effects of the opening characteristics and the draft of the model on wave attenuation functionality and energy dissipation coefficients. Building upon this research, [11] performed a similar experiment, examining the effects on wave energy efficiency and vortex shedding. [12] conducted both experimental and numerical investigations on an L-shaped pile-supported OWC as a breakwater, varying the opening ratio of the orifice and the length of the horizontal bottom plate. [13] followed up with a numerical study on a similar-shaped OWC, but with the bottom horizontal plate detached to reduce the amount of momentum to which the structure is exposed. Furthermore, [14] conducted an analytical study on pile-supported OWCs, exploring the significance of air compressibility at engineering scales. However, it is worth noting that the geometrical optimisation testing of pile-supported OWC designs may not have been adequately explored, which serves as the motivation for this study. Therefore, we have undertaken this study to further expand on this exploration.

This study experimentally examined the hydrodynamic performance of a pile-supported integrated OWC breakwater, incorporating extensive variations in its geometrical parameters. The experiment involved varying parameters such as the opening ratio of the orifice (i.e., the ratio of the orifice cross-sectional area to the cross-sectional area of the pneumatic chamber),

This work was supported in part by the government of Saudi Arabia under the scholarship program through the Ministry of Education.

Yusuf R. Almalki is a Postgraduate researcher at the Department of Civil and Environmental Engineering, Imperial College London, SW7 2AZ, UK (y.almalki20@imperial.ac.uk).

Ioannis Karmpadakis is Coastal Engineering Lecturer at the Department of Civil and Environmental Engineering, Imperial College London, SW7 2AZ, UK (i.karmpadakis@imperial.ac.uk).

Chris Swan is Professor of Hydrodynamics at the Department of Civil and Environmental Engineering, Imperial College London, SW7 2AZ, UK (c.swan@imperial.ac.uk).

Digital Object Identifier:
https://doi.org/10.36688/ewtec-2023-paper-549

the breadth of the chamber, the position of the chamber within the breakwater and the breadth of a front-positioned chamber. The study utilised a novel experimental apparatus that maximises the ability to alter the geometrical characteristics of the model and employs video recording and edge detection techniques to accurately capture the spatial variation of the inner surface elevation, thus enabling an accurate quantification of the power output of the OWC. A total of 16 different design configurations were tested, resulting in a comprehensive dataset of 288 test cases.

The paper is organized as follows: Section II provides a description of the experimental setup, including the instrumentation used and the analysis methodology employed. In Section III, the results are discussed, focusing on the effects of different geometrical parameters on both wave attenuation functionality and energy generation efficiency. Finally, Section IV presents the main conclusions derived from this study.

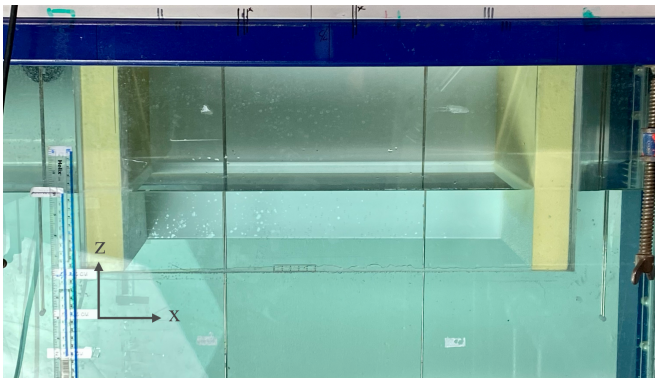

Fig. 1. Photograph showing the scaled physical model installed in the wall–mounted flume.

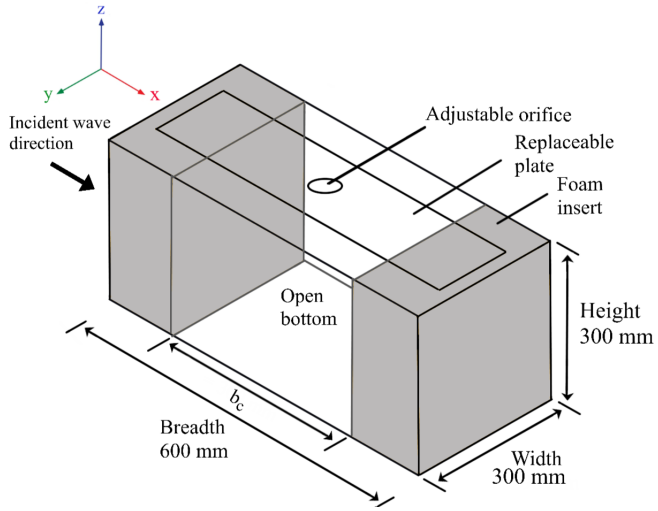

Fig. 2. Geometric details of the physical model.

II. Description of Experiments

A. Physical model and experiment setup

The experiments in this study were conducted using the Wall-mounted flume located in the Hydrodynamic Laboratory at Imperial College London. The flume is a glass-made wave flume with dimensions of $60\,\mathrm{m}$ in length, $0.3\,\mathrm{m}$ in width, and $0.7\,\mathrm{m}$ in depth, and it operates at a depth of $0.5\,\mathrm{m}$.The flume is equipped with a bottom-hinged flap-type wave paddle that has an active absorption capability based on a force-feedback mechanism.

On the downstream end of the flume, an inclined beach with a slope of $1/20$ is installed. To enhance its ability to absorb outgoing waves, the beach is coated with a layer of foam. The effectiveness of this beach configuration was examined, and the results showed an average reflection coefficient of 2% over the testing range of frequencies. For longer wave cases, the maximum reflection coefficient observed was 4% .

The physical model was constructed using Froude number similarity with a length scale of $L_s = 1:20$ and associated time scale of $T_s = 1:\sqrt{20}$. The model was constructed using $5\,\mathrm{mm}$ perspex sheets, which offer visual access to the inner water surface of the chamber. These sheets formed the base frame of the model, with dimensions of $0.3\,\mathrm{m}$ in height, $0.3\,\mathrm{m}$ in width, and $0.6\,\mathrm{m}$ in breadth. A changeable topside lid was incorporated to allow for a variety of top side configurations to be installed. Additionally, a range of foam inserts were designed and used to vary the geometrical parameters of the model. Fig. 1 shows a photograph of the scaled physical model and Fig. 2 presents a sketch with geometric details of the physical model.

To model the PTO mechanism, a circular-shaped orifice was utilised due to its ability to simulate the nonlinear relationship between the air pressure inside the chamber and the airflow discharge across the orifice. The pneumatic power was measured to represent the extracted wave power.

The model used in this experiment was firmly mounted at the top of the flume with a draft of $0.1\,\mathrm{m}$. It was positioned at a distance of $11.35\,\mathrm{m}$ from the wave paddle. A total of 14 resistance-type drop-down wave gauges were used in the experimental setup. Six gauges were placed on the upstream side of the model, maintaining a clearance of approximately $3\,\mathrm{m}$. This placement was intended to prevent contamination from interaction-induced evanescent modes, as these gauges were primarily used to quantify the reflection coefficient. A similar arrangement of wave gauges was installed downstream of the model, primarily utilised to measure the transmission coefficient. Additionally, two wave gauges were attached to the model itself. These gauges served the purpose of measuring the surface elevation inside the pneumatic chamber, allowing for validation of the measurements obtained from camera readings and correction of phase shifting caused by trigger lag. Fig. 3 provides a schematic representation of the experimental arrangement.

In addition, two custom-made differential pressure transducers provided by OMNI instruments were utilised. These transducers were specifically designed to operate within low-pressure ranges, with one covering the range of 0-300 pascal and the other covering 0-500 pascal, offering an improved accuracy with an estimated error of 0.4% of the full scale. These were installed on the model to measure the pneumatic gauge

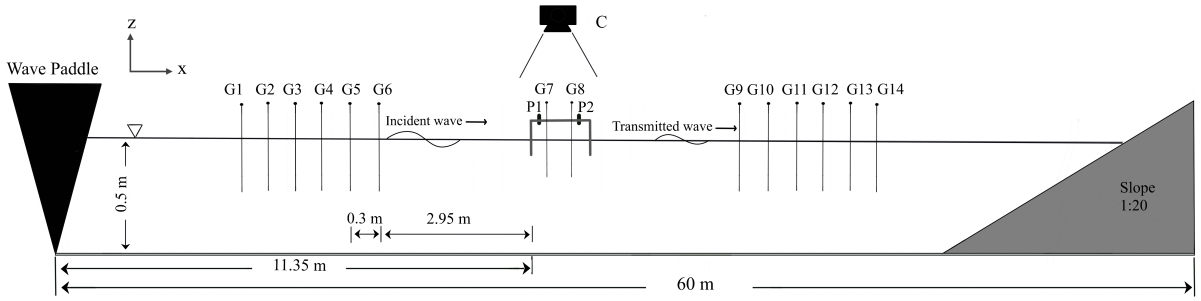

Fig. 3. Schematic of the experimental setup, showing locations of wave gauges (G), pressure transducers (P) and video camera (C).

pressure inside the chamber.

Furthermore, a 4K video recording camera manufactured by SONY was employed. The camera settings were configured to record at 25 frames per second (FS) with high-definition (HD) resolution. These settings were carefully chosen to capture the required data while significantly reducing the computational load during data processing. The camera was positioned to record the side view of the model, enabling the extraction of the inner water surface elevation of the pneumatic chamber. Image processing edge detection techniques were employed to extract the water surface data from the captured images. Fig. 4 illustrates an example of the extracted data using this technique.

The quality of wave generation is of utmost importance when it comes to the successful completion of the present physical model testing. Particular attention has been paid into the correct generation, measurement and analysis of all wave measurements, as described by [15]. Specifically, the wave gauges were calibrated at the start of the experiment and underwent re-calibration each day. Repeatability tests have been conducted and verified the complete reproducibility of results. Following previous works [16], [17], we ensure that our measurement accuracy is contained within $\pm 0.5\,\mathrm{mm}$, beach reflections are below 5% and any unwanted spurious waves are suppressed. Taken together, the resulting dataset represents one of very high quality.

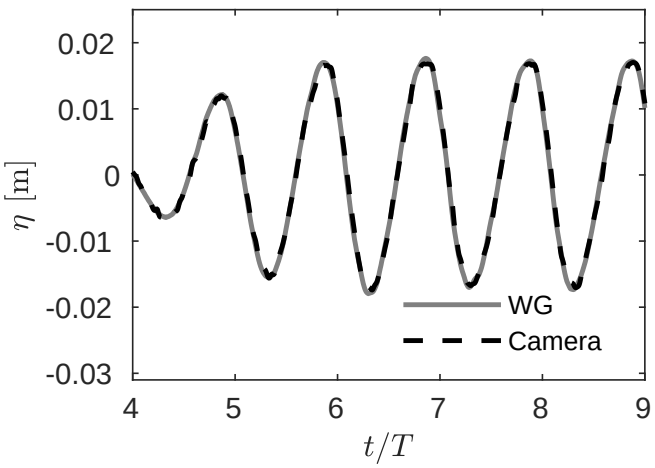

Fig. 4. Surface elevation time-history inside the chamber comparing wave gauge (WG) measurements to camera recordings.

B. Test matrix and wave conditions

The test matrix for this experiment consists of a series of monochromatic wave conditions that span a wide range in the frequency domain; the conditions range between 0.5 and $1.33\,\mathrm{Hz}$. The water depth d was kept at $0.5\,\mathrm{m}$, resulting in a wavelength λ range of $0.88\,\mathrm{m}$ to $4.05\,\mathrm{m}$, with relative breadths ranging from 0.15 to 0.68. Three different wave heights were explored: $H_i = 0.032\,\mathrm{m}$, $0.05\,\mathrm{m}$, and $0.075\,\mathrm{m}$. Detailed information regarding the wave conditions forming the test matrix for this experiment is provided in Table I

TABLE I
WAVE TEST MATRIX

Parameter	Value
H_i	0.032, 0.050, 0.075 m
T	0.75, 1.00, 1.25, 1.50, 1.75, 2.00 s
λ	0.88, 1.51, 2.18, 2.83, 3.45, 4.06 m
$b\lambda^{-1}$	0.68, 0.40, 0.27, 0.21, 0.17, 0.15
d	0.5 m

The experiment investigated various geometrical parameters, including the opening ratio of the orifice, the breadth of the chamber, the position of the chamber within the structure and the breadth of a front-position chamber. These parameters were examined in 16 different configurations, made possible by the flexible nature of the model used. The model allowed for easy changes to the top side configuration and the utilisation of foam inserts, where foam workability was advantageous. Table II provides detailed information on the parameters values that were tested in this experiment.

TABLE II
DETAILS OF GEOMETRIC PARAMETERS UNDER INVESTIGATION

Geometry	Value
Opening ratio, α	0.3, 0.5, 0.6, 0.8, 1 %
Breadth, b	0.6 m
Chamber breadth, b_c	0.1, 0.2, 0.3, 0.4, 0.5, 0.6 m
Chamber position	front, middle, and back

The geometrical parameters were systematically varied in a sequential manner throughout the experiment. Considering the large number of design variables involved in the experiment, we investigate the effects of a single parameter by varying it while all other parameters are kept unchanged. In isolating one parameter at a time we can comment on its impact on the overall efficiency of the device and its coastal

protection potential. In addition, the selection of the parameter space is performed progressively and with the aim to approximate an optimal solution. In other words, once a parameter is tested, the value that performs best is retained for subsequent testing. Strictly speaking, this is only valid if the variables are uncorrelated. Regarding correlated variables alternative methods have been employed to further iterate the design. These go beyond the scope of the present paper but are discussed in an upcoming publication. The present work focuses on the discussion of the effects of parameter variation conditional on a set of values for all other variables.

The testing began by investigating the effect of the opening ratio. It was assumed that the opening ratio is independent of the other geometrical characteristics since it primarily responds to the aerodynamics of the chamber rather than directly to the wave conditions. Next, the breadth of the chamber was examined for a middle chamber configuration. Subsequently, the position of the chamber was tested, revealing that a front-positioned chamber was significantly more efficient. As a result, the breadth chamber of a front-positioned chamber configuration was tested. The position of the chamber and the breadth of the chamber were not assumed to be independent, instead, cross-testing was employed to optimise these two geometrical characteristics.

C. Data acquisition and analysis

The average extracted power output was evaluated by quantifying the average pneumatic power exerted inside the chamber. The latter can be defined from a two-dimensional perspective per unit width as

$$\overline{P}_{owc} = \frac{b_c}{nT} \int_{t_0}^{t_0+nT} p\left(t\right) \frac{d\overline{\eta}_{owc}}{dt} dt \ , \tag{1}$$

where $p\left(t\right)$ represents the instantaneous air pressure inside the pneumatic chamber, T denotes the wave period, b_c represents the breadth of the chamber, and $\overline{\eta}_{owc}$ denotes the instantaneous spatially averaged water surface elevation inside the chamber. The spatially averaged surface elevation was evaluated using the data extracted from video recordings. This approach has the advantage of retaining both the spatial variation and the high-order harmonics resulting in an accurate evaluation of the power output. Conventionally, the spatially averaged surface elevation is quantified by either direct averaging of the wave gauge's readings inside the chamber or by reconstructing the surface elevation from the first harmonics of the incident and reflected wave components.

The energy extraction efficiency ϵ, and the normalised power output $\hat{P}_{owc}$ were defined respectively as

$$\epsilon = \frac{\overline{P}_{owc}}{\overline{P}_i} \ , \tag{2}$$

$$\text{and } \hat{P}_{owc} = \frac{\sum_{n=1}^{N} \overline{P}_{owc\ n}}{\sum_{n=1}^{N} \overline{P}_{i\ n}} \ , \tag{3}$$

where N is the number of test cases under consideration and P_i is the incident wave power per unit width. The latter is given by

$$\overline{P}_i = \frac{1}{8} \rho g H_i^2 C_g \ , \tag{4}$$

where g is the gravitational acceleration, ρ denotes the water density and C_g is the wave group velocity expressed as

$$C_g = \frac{\omega}{2k} \left(1 + \frac{2kd}{\sinh(2kd)}\right) \ . \tag{5}$$

ω denotes the wave angular frequency and k is the wave number, where ω and k satisfy the dispersion relation expressed as

$$\omega^2 = gk \tanh(kd) \ . \tag{6}$$

The reflection coefficient and transmission coefficient are defined respectively by

$$C_r = \frac{H_r}{H_i} \ , \tag{7}$$

$$C_t = \frac{H_t}{H_i} \ . \tag{8}$$

Here, H_r the reflected wave height is evaluated by utilising the least square decomposition method proposed by [18] on the surface elevation readings from gauges 1 to 6, while H_t the transmitted wave height is evaluated by applying the decomposition method to the readings from gauges 9 to 14.

III. Result and discussion

A. Effects of the opening ratio

This section investigates the effects of the opening ratio of the orifice α on energy extraction efficiency, as well as the transmission coefficient and the reflection coefficient. Fig. 5 shows the normalised time-history measurements of the averaged surface elevation, the gauge pressure, and the exerted real-time pneumatic work inside the chamber. The latter was defined in a two-dimensional sense as in Equation (9), while the total energy content in one wavelength is defined as in Equation (10). These measurements are presented for five different values of the opening characteristics. The case depicted in Fig. 5 corresponds to a model with a chamber breadth b_c of $0.3\,\mathrm{m}$, wave period T of $1.5\,\mathrm{s}$, and wave amplitude A_i of $0.016\,\mathrm{m}$.

$$E_{owc}\left(t\right) = b_c \frac{d\overline{\eta}_{owc}\left(t\right)}{dt} p\left(t\right) \tag{9}$$

$$E_i = \rho g \frac{A_i^2 \lambda}{2} \tag{10}$$

Subplot (a) in Fig. 5 illustrates a nearly pure sinusoidal nature for the averaged surface elevation $\overline{\eta}_{owc}$, with a slight phase shift that increases as the opening ratio α decreases. In subplot (b), the pneumatic pressure time-history exhibits a regular wave shape, but with contributions from the third-order harmonic being significant. Subplot (c) displays the real-time pneumatic work, which shows smooth fluctuations from zero to

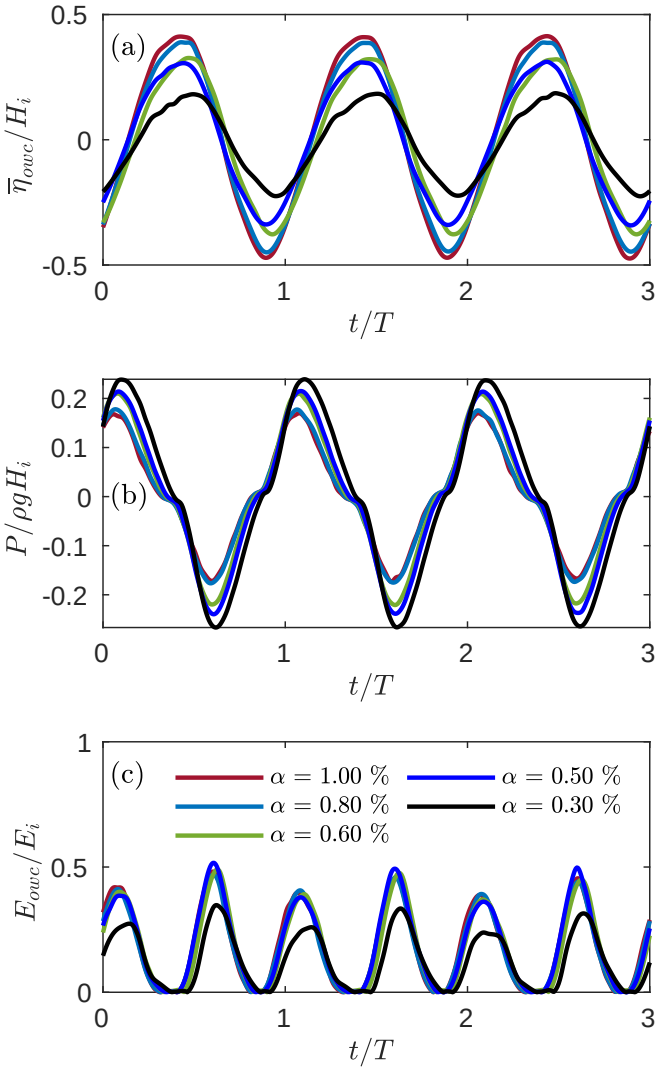

Fig. 5. Data time series showing (a) the normalised spatially average surface elevation inside the chamber, (b) the normalised pneumatic gauge pressure inside the chamber and (c) the instantaneous energy output normalised by the total energy contained in one wavelength.

around 0.4, with larger crests reaching approximately 0.5 every other cycle. This is a result of the suction part of the cycle producing slightly deeper troughs in pressure compared to the compression part of the cycle.

The case with an opening ratio of 0.3% exhibited relatively large pressure fluctuations. However, this did not result in increased energy output since the smaller opening imposed impedance to the surface elevation inside the chamber, allowing it to fluctuate with a relatively small amplitude. The pneumatic pressure fluctuation inside the chamber is induced by the hydraulic resistance of the opening against the air flux across the orifice. Therefore, a smaller opening ratio leads to a larger damping ratio and, consequently, a smaller amplitude for the averaged surface elevation inside the chamber. This behaviour is aligned with the result presented in [19] which found the damping ratio is inversely proportional to the opening ratio.

The largest opening tested here is of α equal to 1%, which exhibited a relatively small pressure amplitude and larger surface elevation fluctuations. Both openings of 0.5% and 0.6% showed approximately similar fluctuation amplitudes with small discrepancies and a slight lead for the 0.5% opening in terms of real-time energy output. It is worth noting that the difference in the real-time energy output for the cases with openings of 1%, 0.8%, 0.6%, and 0.5% was small.

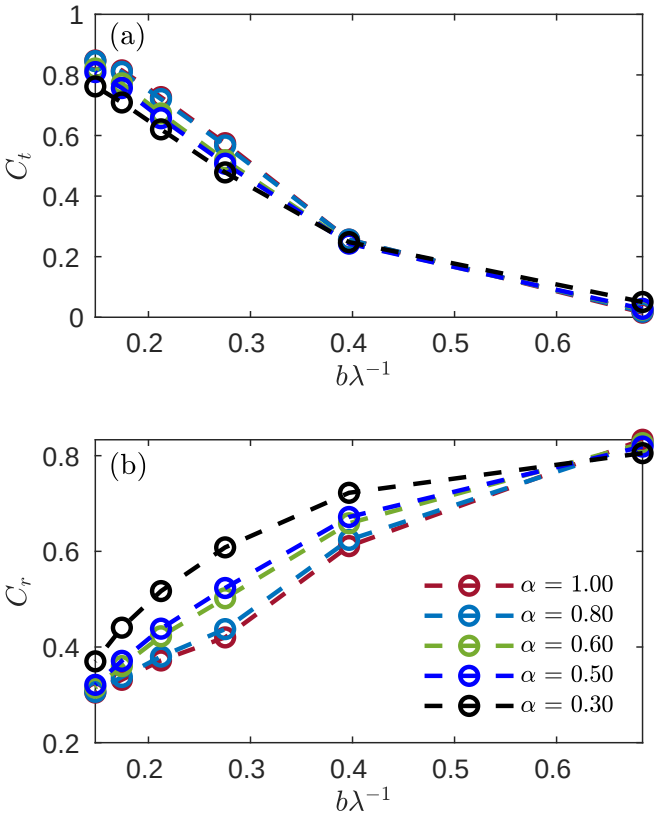

Fig. 6. Effects of the opening ratio α on (a) the transmission coefficient C_t and (b) the reflection coefficient C_r.

Fig. 6 presents the reflection coefficients C_r and transmission coefficients C_t as functions of the relative breadth $b\lambda^{-1}$ for the five opening ratios α of interest. The transmission coefficients show relatively small differences among the opening configurations, with values ranging between 0.84 at a $b\lambda^{-1}$ of 0.15 and 0.02 at a $b\lambda^{-1}$ of 0.68. The smallest transmission coefficient occurs for the smallest opening 0.3 % ratio within the relative breadth range of 0.15 to 0.21, while it induced the largest transmission coefficient observed relative to the rest of the configurations at $b\lambda^{-1}$ of 0.68. However, the minimum transmission coefficient at $b\lambda^{-1}$ of 0.68 is obtained in the case of an opening ratio of 0.5%.

The reflection coefficients, in contrast, showed relatively larger differences among the different configurations compared to the transmission coefficients. The case with a 0.3% opening ratio induced the largest reflection coefficient. From an analytical potential theory perspective, the flow field around an OWC structure can be decomposed into three components: the incident wave field in the absence of the structure, the scattered wave field without the influence of the OWC, and the radiated wave field due to the oscillations of the water column. In this context, the amplitude of the radiated wave is a function of the pressure fluctuation amplitude inside the chamber. The reflected wave amplitude depends on both the scattered and radiated wave

amplitudes and the phase shift between them (see for example [20]). Therefore, an increase in the pressure fluctuation amplitude may result in an increase in the reflection coefficient. This concept explains why the largest reflection coefficients are associated with the $0.3\,\%$ opening ratio case since it induces the largest pressure fluctuation. The openings of $0.5\,\%$ and $0.6\,\%$, exhibited similar trends, as did the $0.8\,\%$ and $1\,\%$ openings, with the overall smallest reflections observed in the $1\,\%$ opening ratio configuration.

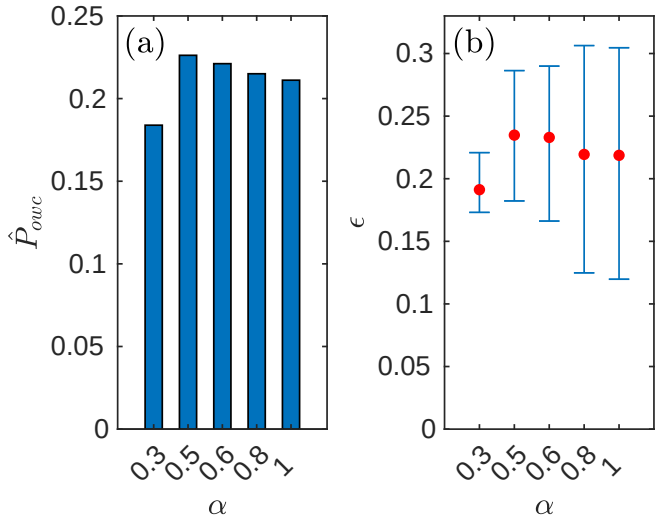

Fig. 7. Effects of the opening ratio α on (a) the normalised power output $\hat{P}_{owc}$ and (b) the energy extraction efficiency coefficient ϵ.

Fig. 7 illustrates the impact of the opening ratio on the normalised power output $\hat{P}_{owc}$ and energy extraction efficiency ϵ across all tested wave cases. Among the opening ratios, the configuration with an opening ratio of $0.5\,\%$ demonstrated the highest energy extraction efficiency, averaging at 0.22 with a maximum value of 0.33.The configurations with opening ratios of $0.5\,\%$, $0.6\,\%$, $0.8\,\%$, and $1\,\%$ performed relatively similarly in terms of the normalised power output, with about $2\,\%$ advantage observed in the $0.5\,\%$ configuration case. It is worth noting that in subplot (b) in Fig. 7 the energy extraction efficiency quantiles span over a wide range of values. This spread is expected since the test matrix included a wide range of wave periods.

In summary, given the negligible differences in transmission coefficients, it can be concluded that the opening ratio $0.5\,\%$ exhibits optimal performance in terms of energy extraction efficiency, making it the overall optimum configuration. It is worth noting that, previous studies conducted by [11], [21], and [12] identified optimal opening ratios of $0.625\,\%$, $0.66\,\%$, and $0.65\,\%$, respectively. However, none of these studies examined an opening ratio of $0.5\,\%$. Nevertheless, these findings are consistent with our results, as the $0.6\,\%$ opening ratio exhibited a very similar energy extraction efficiency to the $0.5\,\%$ configuration, with a slight advantage for the latter.

B. Effects of the breadth of the chamber

This section investigates the effects of the chamber breadth b_c on the hydrodynamic performance of the pile-supported OWC. The objective of this section is to determine the optimal breadth for the OWC relative to a given breakwater geometry, ensuring both effective wave attenuation and energy extraction functionalities. The breadth of the structure remained constant at $0.6\,\mathrm{m}$, while the breadth of the chamber was varied across values of 0.59, 0.5, 0.4, 0.3, 0.2, and $0.1\,\mathrm{m}$. Based on the findings in Subsection III-A, an optimum performance was observed at an opening ratio α of 0.5%. This value was maintained for subsequent experiments. However, as the breadth is being altered in this particular part of the experiment, the orifice size was adjusted accordingly to maintain a constant opening ratio. It is worth noting, that reducing the breadth of the chamber increases the thickness of the front and back drafts. This draft thickness increase introduces a competing effect that occurs simultaneously with the effect of the breadth of the chamber. However, this specific aspect will be resolved when investigating the effect of the position of the chamber within the breakwater in Subsection III-C where the draft thickness will be placed both in the front or at the back of the model.

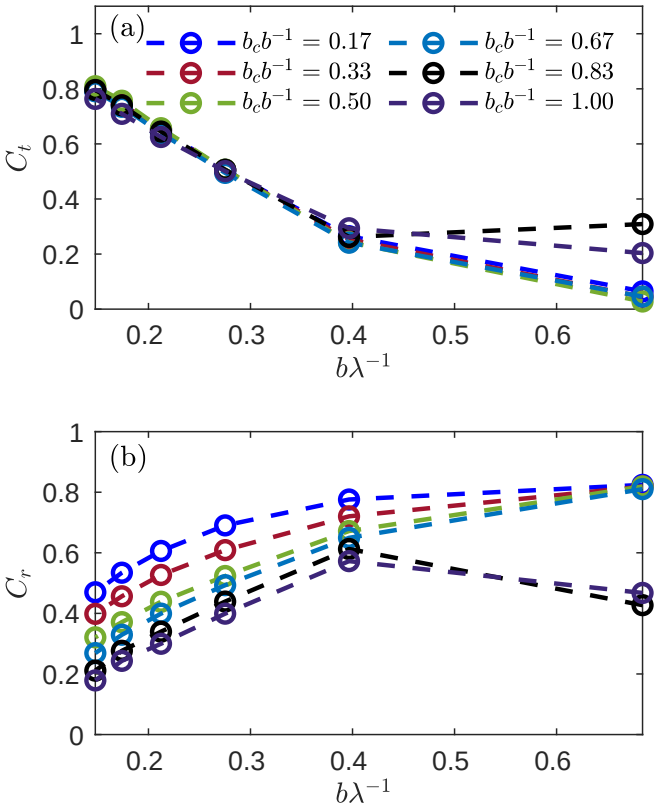

Fig. 8. Effects of the relative chamber breadth b_cb^{-1} on (a) the transmission coefficient C_t and (b) the reflection coefficient C_r.

Fig. 8 shows the influence of the relative chamber breadth b_cb^{-1} on the reflection coefficient C_r and transmission coefficient C_t as a function of the relative breadth $b\lambda^{-1}$ for the six different chamber breadth configurations. It was observed that the differences in the transmission coefficients among the tested cases were relatively small compared to the differences in the reflection coefficients. The transmission coefficients C_t exhibited similar decreasing trends across the different configurations. The transmission coefficients

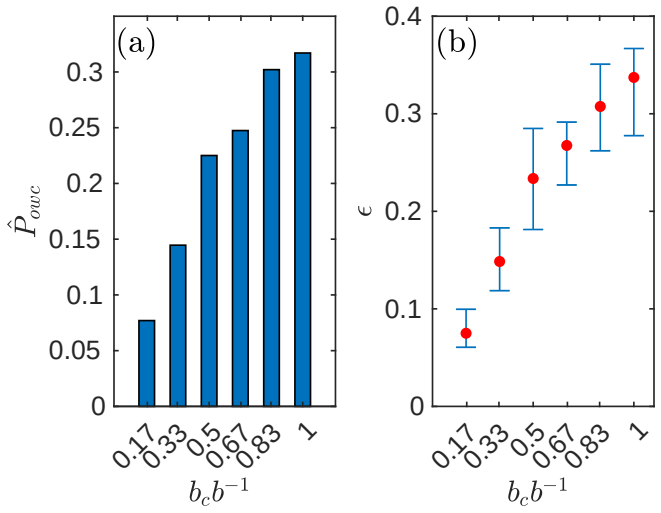

Fig. 9. Effects of the relative chamber breadth $b_c b^{-1}$ on (a) the normalised power output $\hat{P}_{owc}$ and (b) the energy extraction efficiency coefficient ϵ.

peaked at 0.81 for a relative breadth $b\lambda^{-1}$ of 0.15 and a relative chamber breadth $b_c b^{-1}$ of 0.5. Furthermore, they reached a minimum value of 0.027 for a relative breadth $b\lambda^{-1}$ of 0.68 and a relative chamber breadth $b_c b^{-1}$ of 0.5. The decreasing trends were consistent, except for two test cases where the relative chamber breadth $b_c b^{-1}$ was equal to 0.83 and 1 at a relative breadth $b\lambda^{-1}$ of 0.68. In these cases, the excitation of the sloshing mode occurred. This mode induces wall-to-wall motion of the water, similar to enclosed tank sloshing modes, leading to a significant reduction in the energy extraction efficiency, as well as a reduction in the reflection coefficient. Such phenomena can be observed when the relative breadth $b\lambda^{-1}$ is close to 0.5, as highlighted in the studies by [20], and [10].

On the other hand, the reflection coefficients C_r exhibited more spaced curves. Overall, larger reflection coefficients were associated with a relative chamber breadth $b_c b^{-1}$ of 0.17, while the smallest reflection coefficients were associated with a relative chamber breadth $b_c b^{-1}$ of 1.

Fig. 9 depicts the influence of the relative chamber breadth $b_c b^{-1}$ on the normalised power output $\hat{P}_{owc}$ and energy extraction efficiency ϵ for all tested wave cases. The normalised power output demonstrates an increasing trend as the breadth of the chamber increases, reaching a peak value of 0.32 when the relative chamber breadth $b_c b^{-1}$ is 1. Conversely, the minimum value of 0.08 is observed for a relative chamber breadth $b_c b^{-1}$ of 0.17. The energy extraction efficiency ϵ was found to peak for the individual wave cases at a relative chamber breadth $b_c b^{-1}$ of 1.

C. Effects of the chamber position

This section investigates the impact of positioning the pneumatic chamber within the breakwater on energy extraction efficiency, as well as the transmission coefficient and reflection coefficient. While the Subsection III-B highlighted a structure with a relative chamber breadth $b_c b^{-1}$ of 1 as an optimal choice, particularly in terms of energy extraction efficiency, further investigation is necessary to assess the influence of draft thickness and explore cases with displaced pneumatic chambers from the centre. To accomplish this, three different configurations were selected for testing: a) a front-positioned pneumatic chamber, b) a middle-positioned pneumatic chamber, and c) a back-positioned pneumatic chamber, as depicted in Fig. 10. In these cases, the breadth of the structure b remained constant at $0.6\,\mathrm{m}$, while the chamber breadth b_c was set to $0.4\,\mathrm{m}$.

Fig. 11 demonstrates the impact of positioning the pneumatic chamber within the breakwater on the reflection coefficient C_r and transmission coefficient C_t as a function of the relative breadth $b\lambda^{-1}$ for the three tested configurations. Similar to the observation in Subsection III-B regarding the effect of chamber breadth, it was observed that the differences in the transmission coefficients among the tested cases were relatively small compared to the differences in the reflection coefficients. The transmission coefficients C_t exhibited a decreasing trend across the different configurations reaching a peak value of 0.79 for a relative breadth $b\lambda^{-1}$ of 0.15 in the middle-positioned configuration, and a minimum value of 0.046 was observed at a relative breadth $b\lambda^{-1}$ of 0.68 for the middle-positioned configuration. In contrast, the reflection coefficients C_r exhibited divergent trends, with generally smaller reflection coefficients observed in the front-positioned configuration and larger reflection coefficients associated with the back-positioned chamber configuration.

Fig. 12 depicts the impact of the positioning of the pneumatic chamber on the normalised power output $\hat{P}_{owc}$ and energy extraction efficiency ϵ for all tested wave cases. The front-positioned chamber configuration exhibited significantly higher normalised power output $\hat{P}_{owc}$ of 0.33 and maximum efficiency ϵ of 0.53, while the back-positioned chamber configuration showed the lowest normalised power output $\hat{P}_{owc}$ of 0.20 with a maximum efficiency ϵ of 0.30. The front draft acted as a reflector positioned in front of the chamber, leading to a decrease in the proportion of energy that the OWC was exposed to in the cases of the middle-positioned chamber and back-positioned chamber. This observation can provide an explanation for the trends observed in the energy extraction efficiency as depicted in Fig. 12 and the trends of reflection coefficients that are shown in Fig. 11.

D. Effects of the chamber breadth in a front-positioned configuration

Based on the findings presented in Subsection III-C, which demonstrated that the front-positioned chamber configuration outperformed its counterparts, particularly in terms of the energy extraction efficiency ϵ, this section aims to explore the impact of chamber breadth b_c in a front-positioned chamber configuration on the energy extraction efficiency, as well as the transmission coefficient and reflection coefficient. The objective is to identify the optimal breadth of the OWC in relation to a specific breakwater geometry, considering both effective wave attenuation and energy

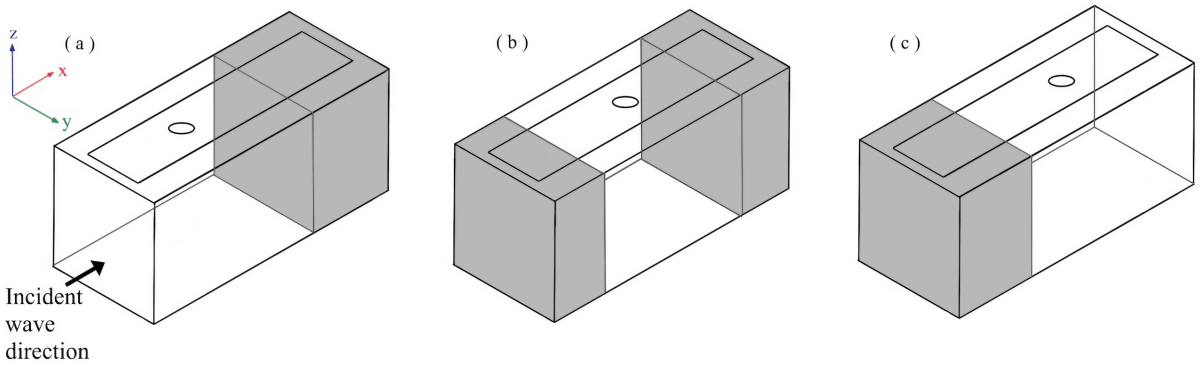

Fig. 10. Schematic of (a) the front-positioned chamber configuration, (b) the middle-positioned chamber configuration and (c) the back-positioned chamber configuration.

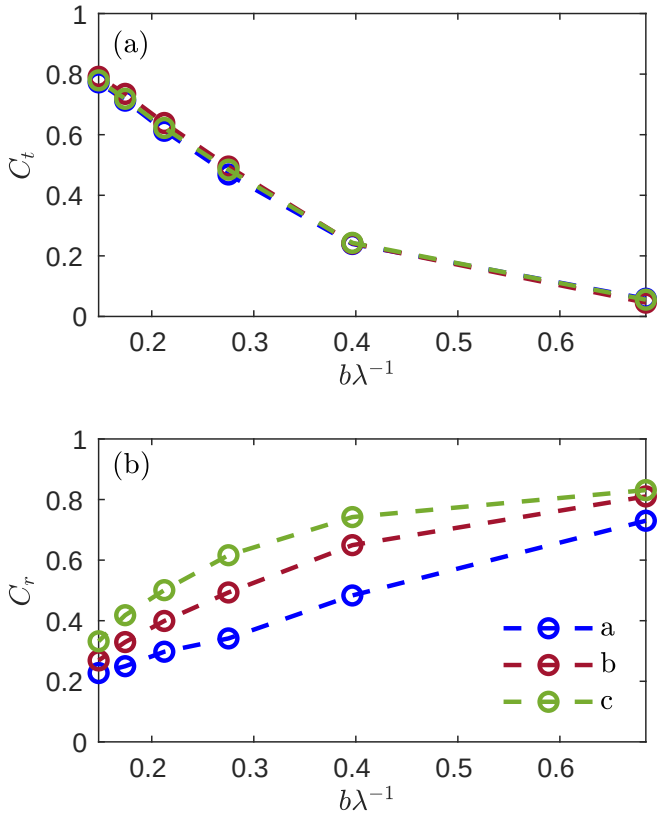

Fig. 11. Effects of the position of the chamber within the breakwater on (a) the transmission coefficient C_t and (b) the reflection coefficient C_r.

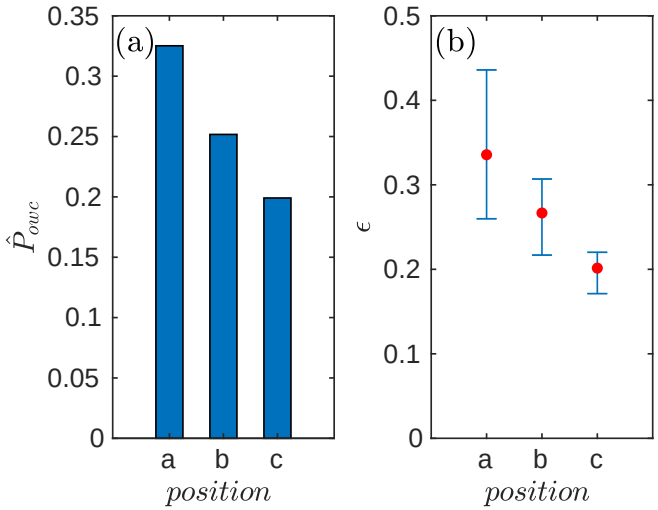

Fig. 12. Effects of the position of the chamber within the breakwater on (a) the normalised power output $\hat{P}_{owc}$ and (b) the energy extraction efficiency coefficient ϵ.

extraction functionalities. The chamber breadth was adjusted following a similar approach to that employed in Subsection III-B, with the orifice size being adjusted accordingly to maintain a constant opening ratio α of 0.5%.

Fig. 13 illustrates the impact of the relative chamber breadth $b_c b^{-1}$ on the reflection coefficient C_r and transmission coefficient C_t as a function of the relative breadth $b\lambda^{-1}$ for the six different chamber breadth configurations. It was observed that the differences in the transmission coefficients among the tested cases were relatively small compared to the differences in the reflection coefficients. Notably, the two cases with relative chamber breadth of $b_c b^{-1}$ equal to 0.83, and 1 exhibited a distinct behaviour at $b\lambda^{-1}$ of 0.68, due to the excitation of the sloshing mode, similar to the case mentioned in Subsection III-B.

Fig. 14 depicts the influence of the relative chamber breadth $b_c b^{-1}$ on the normalised power output $\hat{P}_{owc}$ and energy extraction efficiency ϵ for all tested wave cases. Interestingly, it was observed that the normalised power output reached a peak value of 0.33 at a relative chamber breadth $b_c b^{-1}$, unlike in Subsection III-C, of 0.67, with a maximum efficiency of 0.53. On the other hand, the widest chamber exhibited a normalised power output of 0.32, with a maximum efficiency recorded at 0.42. Notably, the performance of the 0.5 relative chamber breadth was very close to that of the 0.83 relative chamber breadth, with a 2% difference in normalised power output and a slight advantage to the relative chamber breadth of 0.5 in terms of maximum energy extraction efficiency. According to linear potential theory for OWCs (e.g., [20]), a wider pneumatic chamber increases the potential power extraction efficiency. However, the observations in this subsection can be explained by the competing effect of the presence of the back draft acting as a reflector. In cases with a thicker back draft, the energy potential exposed to the OWC increases. In summary,

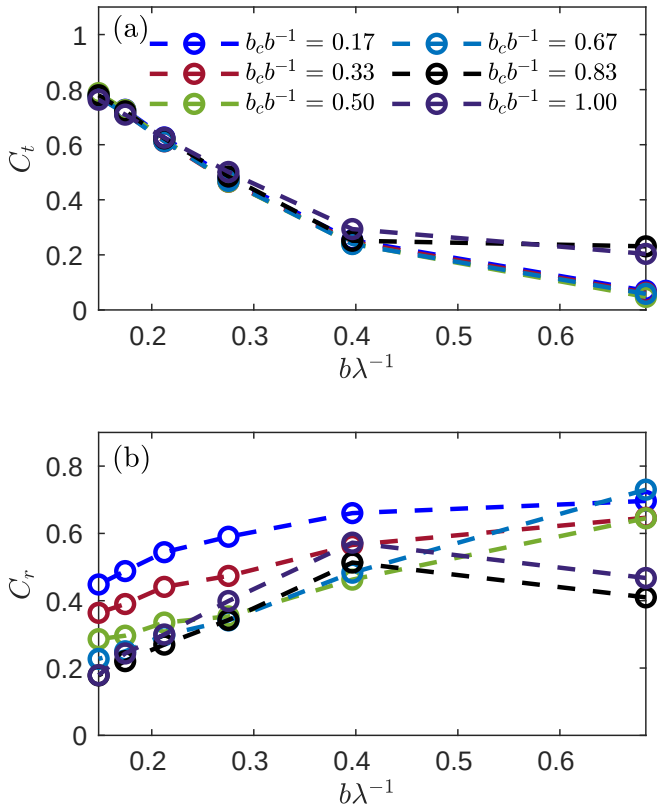

Fig. 13. Effects of the relative chamber breadth $b_c b^{-1}$ in a front-positioned chamber configuration on (a) the transmission coefficient C_t and (b) the reflection coefficient C_r.

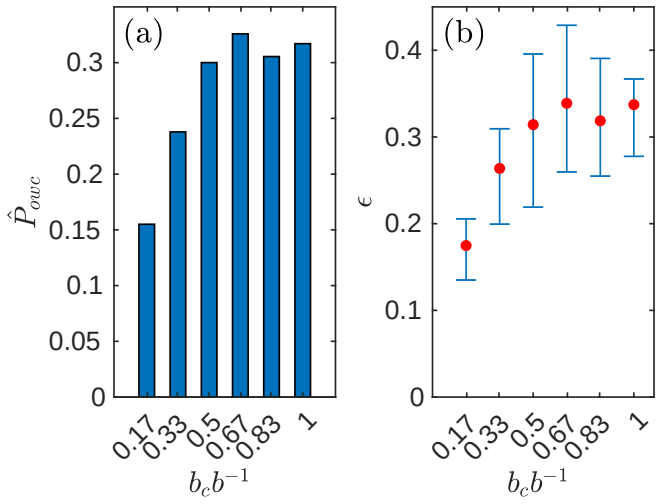

Fig. 14. Effects of the relative chamber breadth $b_c b^{-1}$ in a front-positioned chamber configuration on (a) the normalised power output $\hat{P}_{owc}$ and (b) the energy extraction efficiency coefficient ϵ.

the configuration with a relative chamber breadth of 0.67 was identified as the optimum choice in terms of both energy extraction efficiency and transmission coefficient.

IV. Conclusion

The current study employed laboratory experiments to evaluate the influence of geometrical parameters on the hydrodynamic performance of an integrated pile-supported OWC breakwater. The physical model design implemented Froude similarity with a length scale of $L_s = 1 : 20$. The experimental setup incorporated edge detection techniques applied to video recordings of the model's side view, which enabled capturing both spatial variations and contributions from higher harmonics. From this study, the following conclusions can be drawn:

- The overall hydrodynamic efficiency of a pile-support OWC, can significantly be improved by systematically fine-tuning its geometrical parameters.
- An opening ratio α of $0.5\,\%$ was demonstrated to achieve an effective energy extraction, while the performance differences in the opening ratios ranged from $0.5\,\%$ to $1\,\%$ observed to be small.
- A front-positioned chamber configuration significantly improved the performance of the OWC since the back draft acted as a reflector and increased the potential energy that is exposed to the OWC.
- A front-positioned chamber with a relative chamber breadth $b_c b^{-1}$ of 0.67 demonstrated superior performance compared to wider configurations, both in terms of leveraging energy extraction efficiency and reducing the transmission coefficient.

In summary, the integrated pile-supported OWC breakwater exhibits significant potential as a multi-use structure, providing shelter for shore and harbour activities while efficiently generating energy.

References

[1] F. He, Z. Huang, and A. W.-K. Law, "Hydrodynamic performance of a rectangular floating breakwater with and without pneumatic chambers: An experimental study," *Ocean Engineering*, vol. 51, pp. 16–27, 2012. [Online]. Available: https://www.sciencedirect.com/science/article/pii/S0029801812001692

[2] R. Ojima, S. Suzumura, and Y. Goda, "Theory and experiments on extractable wave power by an oscillating water-column type breakwater caisson," *Coastal engineering in Japan*, vol. 27, no. 1, pp. 315–326, 1984. [Online]. Available: https://www.tandfonline.com/doi/abs/10.1080/05785634.1984.11924396

[3] S. Takahashi, H. Nakada, H. Ohneda, and M. Shikamori, "Wave power conversion by a prototype wave power extracting caisson in sakata port," in *Coastal Engineering 1992*, 1992, pp. 3440–3453. [Online]. Available: https://ascelibrary.org/doi/abs/10.1061/9780872629332.261

[4] K. Thiruvenkatasamy and S. Neelamani, "On the efficiency of wave energy caissons in array," *Applied Ocean Research*, vol. 19, no. 1, pp. 61–72, 1997. [Online]. Available: https://www.sciencedirect.com/science/article/pii/S0141118797000084

[5] R.-S. Tseng, R.-H. Wu, and C.-C. Huang, "Model study of a shoreline wave-power system," *Ocean Engineering*, vol. 27, no. 8, pp. 801–821, 2000. [Online]. Available: https://www.sciencedirect.com/science/article/pii/S0029801899000281

[6] P. Boccotti, P. Filianoti, V. Fiamma, and F. Arena, "Caisson breakwaters embodying an owc with a small opening—part ii: A small-scale field experiment," *Ocean Engineering*, vol. 34, no. 5-6, pp. 820–841, 2007. [Online]. Available: https://www.sciencedirect.com/science/article/pii/S002980180600165X

[7] P. Boccotti, "Design of breakwater for conversion of wave energy into electrical energy," *Ocean engineering*, vol. 51, pp. 106–118, 2012. [Online]. Available: https://www.sciencedirect.com/science/article/pii/S0029801812001722

[8] A. J. Sarmento, "Wave flume experiments on two-dimensional oscillating water column wave energy devices," *Experiments in Fluids*, vol. 12, no. 4-5, pp. 286–292, 1992. [Online]. Available: https://doi.org/10.1007/BF00187307

[9] A. J. N. A. Sarmento and A. F. d. O. Falcão, "Wave generation by an oscillating surface-pressure and its application in wave-energy extraction," *Journal of Fluid Mechanics*, vol. 150, p. 467–485, 1985.

[10] F. He and Z. Huang, "Hydrodynamic performance of pile-supported OWC-type structures as breakwaters: An experimental study," *Ocean Engineering*, vol. 88, pp. 618–626, 2014. [Online]. Available: http://dx.doi.org/10.1016/j.oceaneng.2014.04.023

[11] F. He, M. Li, and Z. Huang, "An experimental study of pile-supported owc-type breakwaters: energy extraction and vortex-induced energy loss," *Energies*, vol. 9, no. 7, p. 540, 2016. [Online]. Available: https://www.mdpi.com/147712

[12] Z. Deng, C. Wang, P. Wang, P. Higuera, and R. Wang, "Hydrodynamic performance of an offshore-stationary owc device with a horizontal bottom plate: Experimental and numerical study," *Energy*, vol. 187, p. 115941, 2019. [Online]. Available: https://www.sciencedirect.com/science/article/pii/S0360544219316251

[13] C. Wang and Y. Zhang, "Hydrodynamic performance of an offshore oscillating water column device mounted over an immersed horizontal plate: A numerical study," *Energy*, vol. 222, p. 119964, 2021. [Online]. Available: https://www.sciencedirect.com/science/article/pii/S0360544221002139

[14] F. He, H. Zhang, J. Zhao, S. Zheng, and G. Iglesias, "Hydrodynamic performance of a pile-supported owc breakwater: An analytical study," *Applied Ocean Research*, vol. 88, pp. 326–340, 2019. [Online]. Available: https://www.sciencedirect.com/science/article/pii/S0141118719300719

[15] I. Karmpadakis, C. Swan, and M. Christou, "Laboratory investigation of crest height statistics in intermediate water depths," *Proceedings of the Royal Society A: Mathematical, Physical and Engineering Sciences*, vol. 475, p. 20190183, 9 2019. [Online]. Available: https://royalsocietypublishing.org/doi/10.1098/rspa.2019.0183

[16] I. Karmpadakis and C. Swan, "On the average shape of the largest waves in finite water depths," *Journal of Physical Oceanography*, vol. 50, pp. 1023–1043, 4 2020. [Online]. Available: https://journals.ametsoc.org/view/journals/phoc/50/4/jpo-d-19-0165.1.xml

[17] ——, "A new crest height distribution for nonlinear and breaking waves in varying water depths," *Ocean Engineering*, vol. 266, p. 112972, 2022. [Online]. Available: https://www.sciencedirect.com/science/article/pii/S0029801822022557

[18] C.-Y. Lin and C.-J. Huang, "Decomposition of incident and reflected higher harmonic waves using four wave gauges," *Coastal engineering*, vol. 51, no. 5-6, pp. 395–406, 2004. [Online]. Available: https://www.sciencedirect.com/science/article/pii/S0378383904000535

[19] A. Çelik and A. Altunkaynak, "Determination of hydrodynamic parameters of a fixed owc by performing experimental and numerical free decay tests," *Ocean Engineering*, vol. 204, p. 106827, 2020. [Online]. Available: https://www.sciencedirect.com/science/article/pii/S0029801819309254

[20] D. Evans and R. Porter, "Hydrodynamic characteristics of an oscillating water column device," *Applied Ocean Research*, vol. 17, no. 3, pp. 155–164, 1995. [Online]. Available: https://www.sciencedirect.com/science/article/pii/0141118795000089

[21] D.-Z. Ning, R.-Q. Wang, Y. Gou, M. Zhao, and B. Teng, "Numerical and experimental investigation of wave dynamics on a land-fixed owc device," *Energy*, vol. 115, pp. 326–337, 2016. [Online]. Available: https://www.sciencedirect.com/science/article/pii/S0360544216312324